The Astronomical Journal, 158:76 (14pp), 2019 August https://doi.org/10.3847/1538-3881/ab2d20

ALMA Spectral Imaging of Titan Contemporaneous with *Cassini*'s Grand Finale

M. A. Cordiner[1,2], N. A. Teanby[3], C. A. Nixon[1], V. Vuitton[4], A. E. Thelen[1,2], and S. B. Charnley[1]
[1] NASA Goddard Space Flight Center, 8800 Greenbelt Road, MD 20771, USA; martin.cordiner@nasa.gov
[2] Institute for Astrophysics and Computational Sciences, The Catholic University of America, Washington, DC 20064, USA
[3] School of Earth Sciences, University of Bristol, Wills Memorial Building, Queens Road, Bristol, BS8 1RJ, UK
[4] Université Grenoble Alpes, CNRS, IPAG, F-38000 Grenoble, France
Received 2019 March 20; revised 2019 June 20; accepted 2019 June 25; published 2019 July 24

Abstract

The *Cassini* mission performed 127 targeted flybys of Titan during its 13 yr mission to Saturn, culminating in the Grand Finale between 2017 April and September. Here we demonstrate the use of the Atacama Large Millimeter/submillimeter Array (ALMA) to continue *Cassini*'s legacy for chemical and climatological studies of Titan's atmosphere. Whole-hemisphere, interferometric spectral maps of HCN, HNC, HC_3N, CH_3CN, C_2H_3CN, C_2H_5CN, and C_3H_8 were obtained using ALMA in 2017 May at moderate ($\approx 0\farcs2$, or $\approx$1300 km) spatial resolution, revealing the effects of seasonally variable chemistry and dynamics on the distribution of each species. The ALMA submillimeter observations of HCN and HC_3N are consistent with *Cassini* infrared data on these species, obtained in the same month. Chemical/dynamical lifetimes of a few years are inferred for C_2H_3CN and C_2H_5CN, in reasonably close agreement with the latest chemical models incorporating the sticking of C_2H_5CN to stratospheric aerosol particles. ALMA radial limb flux profiles provide column density information as a function of altitude, revealing maximum abundances in the thermosphere (above 600 km) for HCN, HNC, HC_3N, and C_2H_5CN. This constitutes the first detailed measurement of the spatial distribution of HNC, which is found to be confined predominantly to altitudes above 730 ± 60 km. The HNC emission map shows an east–west hemispheric asymmetry of $13\% \pm 3\%$. These results are consistent with very rapid production (and loss) of HNC in Titan's uppermost atmosphere, making this molecule an effective probe of short-timescale (diurnal) ionospheric processes.

Key words: planets and satellites: atmospheres – planets and satellites: individual (Titan) – submillimeter: planetary systems – techniques: imaging spectroscopy – techniques: interferometric

1. Introduction

Saturn's largest moon Titan has a thick (1.45 bar) atmosphere composed primarily of molecular nitrogen (98%) and methane (~2%). Remote and in situ measurements have identified a wealth of other species therein (see Bézard et al. 2014), the abundances, distributions, and temperatures of which are linked to seasonal variations in Titan's combined photochemistry and atmospheric circulation patterns (e.g., Teanby et al. 2009; Vinatier et al. 2010; Achterberg et al. 2011; Cordiner et al. 2015; Thelen et al. 2019). Hydrocarbons and nitriles spanning a broad range in size and complexity have been detected, from acetylene (C_2H_2) and hydrogen cyanide (HCN) to benzene (C_6H_6), propionitrile (CH_2CH_3CN), and organic aerosols (Hörst 2017), which are theorized to originate from photochemistry initiated primarily by N_2 and CH_4 photolysis in the upper atmosphere (Vuitton et al. 2019). However, despite 13 years of dedicated study by the *Cassini* spacecraft during over 120 scientific flybys (from 2004 to 2017), major gaps remain in our knowledge of Titan's atmospheric chemistry and dynamics (Hörst 2017; Nixon et al. 2018), particularly regarding the sources and sinks of complex organic molecules.

Strong latitudinal anisotropies in the abundances of Titan's smaller hydrocarbons and nitriles (such as HCN, HC_3N, and C_2H_2) were first observed by *Voyager 1* (Coustenis & Bezard 1995). Continued monitoring of these and other species by the *Cassini* Composite Infrared Spectrometer (CIRS) has revealed temporal variations in the abundance patterns of photochemically produced gases over time periods as short as (Earth) years or even months (Teanby et al. 2012, 2017; Coustenis et al. 2013; Vinatier et al. 2015). The observed changes in molecular distributions are unique among the bodies of the solar system and are believed to be driven by seasonal insolation variations, mediated by a global meridional circulation cell that changes direction during Titan's 29.5 yr seasonal cycle. To provide new insights into Titan's atmospheric chemistry and global circulation system, we undertook a program to perform the comprehensive mapping of short-lived photochemical products using the Atacama Large Millimeter/submillimeter Array (ALMA) and *Cassini* CIRS during the transition to Titan's northern summer solstice in 2017 May. These observations capitalize on (1) the recent completion of the full array of 50×12 m ALMA antennas, enabling the highest-resolution studies of Titan to date at millimeter/submillimeter wavelengths (see also Lellouch et al. 2019), and (2) the final opportunity for contemporaneous observations using ALMA and CIRS. The aim of this study was to combine the complementary diagnostic power of the submillimeter and infrared spectral regions to provide the most complete picture to date of Titan's rapidly evolving chemistry and dynamics.

Cassini CIRS spectroscopy benefits from high sensitivity and spatial resolution for measuring rovibrational molecular emission lines, but provides an incomplete picture of Titan, hindered by a relatively low spectral resolution ($R \sim 2000$) and reduced sensitivity at far-infrared wavelengths. Moreover, CIRS is only sensitive to a subset of Titan's gases (including CO, HCN, H_2O, HC_3N, C_2N_2, and various C_nH_m hydrocarbons), and crucially, lacks the ability to detect several important and abundant nitrogen-bearing species. Polar nitriles (such as HNC, HC_3N, C_2H_5CN, and C_2H_3CN) are among the species with the shortest predicted chemical lifetimes (less than a few years in the stratosphere; see Wilson & Atreya 2004; Krasnopolsky 2009; Vuitton et al. 2019) and are therefore

extremely useful probes of Titan's short-timescale atmospheric variability. The millimeter/submillimeter wavelength regime provides optimal sensitivity for rotational emission from polar nitriles, and with its combined high sensitivity and spatial resolution, ALMA can provide detailed maps of the emission from these species in Titan's atmosphere. Through radiative transfer analysis, the combined *Cassini* plus ALMA data set enables molecular abundances to be derived as a function of spatial coordinate, from which a comprehensive evaluation of our understanding of the dominant nitrile formation and destruction pathways in nitrogen- and carbon-rich planetary atmospheres can be obtained. Such information is crucial for constraining theories regarding the formation of aerosols and complex nitrogen-bearing organics (including possible prebiotic species) in primitive (exo)planetary atmospheres throughout the Galaxy.

The observations presented here provide an overview of the complete ALMA data set obtained in synergy with the final Titan flybys by *Cassini*. Molecular maps for HCN, HNC, HC_3N, CH_3CN, C_2H_3CN, C_2H_5CN, and C_3H_8 demonstrate ALMA's unique, high-sensitivity interferometric imaging capabilities, resulting in spatially resolved distributions for individual molecules, from which we derive preliminary abundances and chemical/dynamical decay timescales. By comparison with results from the latest atmospheric chemical models, new insights are obtained into the relationship between Titan's climate, chemistry, and global atmospheric circulation system.

2. ALMA Observations

Observations of Titan were carried out using the ALMA Band 7 receiver on 2017 May 8 and 16, as part of the director's discretionary time program 2016.A.00014.S. The observations were targeted to be close in time to *Cassini*'s May 24 (solstice) flyby of Titan, for synergistic observations with CIRS. The ALMA correlator was configured using two different spectral settings to observe multiple frequency windows covering our molecules of interest in the ranges (1) 342–356 GHz (877–842 μm) and (2) 349–364 GHz (859–824 μm), at a spectral resolution of 244–977 kHz (0.2–0.8 km s^{-1}). For more details of the targeted spectral lines, see Table 1.

The ALMA configuration was moderately extended, with 46 active antennas providing baselines in the range of 15–1124 m, resulting in a spatial resolution of $\approx 0\farcs2$ (using natural visibility weighting). The total on-source observing time was 18 minutes in setting 1 and 138 minutes in setting 2, leading to rms noise levels in the range of 2–4 mJy beam^{-1} MHz^{-1}. Weather conditions were very good, with zenith precipitable water vapor in the range of 0.74–0.83 mm, resulting in low atmospheric opacity and good phase stability.

After the initial calibration of the antenna phase delays, the observations consisted of bandpass and flux calibration scans, followed by an interleaved sequence of three visits each to Titan and the phase calibrator J1751–1950. The phase center was updated in real time to track Titan's moving position on the sky. The flux of the calibration quasar J1733–1304 was measured on 2017 May 4 and 17, with an accuracy of $\pm 6\%$, implying a similar accuracy in the flux scale of our calibrated spectra.

Data were flagged and calibrated in CASA 5.1 (Jaeger 2008) using the automated pipeline scripts supplied by the Joint ALMA Observatory (see Shinnaga et al. 2015). The data from May 8 and 16 were combined after regridding and Doppler-shifting to Titan's rest frame. A small offset in decl. (of unknown origin) was identified and corrected in Titan's position with respect to the ALMA phase center on May 8 ($0\farcs06$ in setting 1 and $0\farcs11$ in setting 2). Titan's continuum flux was subtracted using low-order polynomial fits to the (line-free) spectral regions adjacent to our lines of interest. Imaging and deconvolution were

Table 1
ALMA Detected Emission Line Frequencies, Transitions, and Upper-state Energies

Species	Rest Freq. (MHz)	Transition	Spec. Res. (kHz)	E_u (K)
CO	345796	3–2	977	33.2
HCN	354505	4–3	977	42.5
HCN	354460	4–3, $v_2 = 1e$	977	1067
HNC	362630	4–3	244	42.5
$H^{13}CN$	345340	4–3	977	41.4
$H^{13}CN$	345239	4–3, $v_2 = 1e$	977	1057
$HC^{15}N$	344200	4–3	977	41.3
HC_3N	345609	38–37	977	324
HC_3N	354697	39–38	977	341
HC_3N	355278	39–38, $v_6 = 1e$	977	1059
HC_3N	355557	39–38, $v_6 = 1f$	977	1059
HC_3N	355566	39–38, $v_7 = 1e$	977	662
HC_3N	356072	39–38, $v_7 = 1f$	977	662
HC_3N	363785	40–39	244	358
$H^{13}CCCN$	343739	39–38	977	330
$H^{13}CCCN$	361353	41–40	488	364
$HC^{13}CCN$	344143	38–37	977	322
$HC_3^{15}N$	344385	39–38	977	331
CH_3CN	349025	19_8–18_8	488	624
CH_3CN	349125	19_7–18_7	488	517
CH_3CN	349212	19_6–18_6	488	425
CH_3CN	349286	19_5–18_5	488	346
CH_3CN	349346	19_4–18_4	488	282
CH_3CN	349393	19_3–18_3	488	232
CH_3CN	349427	19_2–18_2	488	196
CH_3CN	349447	19_1–18_1	488	175
CH_3CN	349454	19_0–18_0	488	168
$CH_3^{13}CN$	349221	19_3–18_3	488	232
$CH_3^{13}CN$	349254	19_2–18_2	488	196
$CH_3^{13}CN$	349274	19_1–18_1	488	175
$CH_3^{13}CN$	349280	19_0–18_0	488	168
C_2H_3CN	360876	$38_{8,31}$–$37_{8,30}$	488	476
C_2H_3CN	360876	$38_{8,30}$–$37_{8,29}$	488	476
C_2H_3CN	360878	$38_{9,29}$–$37_{9,28}$	488	512
C_2H_3CN	360878	$38_{9,30}$–$37_{9,29}$	488	512
C_2H_3CN	361652	$38_{4,35}$–$37_{4,34}$	488	373
C_2H_5CN	343195	$38_{5,33}$–$37_{5,32}$	977	347
C_2H_5CN	354477	$40_{3,38}$–$39_{3,37}$	977	361
C_2H_5CN	355756	$39_{3,36}$–$38_{3,35}$	977	351
C_2H_5CN	349443	$39_{10,30}$–$38_{10,29}$	488	446
C_2H_5CN	349443	$39_{10,29}$–$38_{10,28}$	488	446
C_2H_5CN	349547	$39_{9,31}$–$38_{9,30}$	488	425
C_2H_5CN	349547	$39_{9,30}$–$38_{9,29}$	488	425
C_2H_5CN	349731	$39_{8,32}$–$38_{8,31}$	488	407
C_2H_5CN	349731	$39_{8,31}$–$38_{8,30}$	488	407
C_2H_5CN	349796	$39_{4,36}$–$38_{4,35}$	488	354
C_3H_8	360978	8_6–7_5	488	64.2

Note. Transitions are expressed as $J' - J''$, $J'_{K'} - J''_{K''}$ or $J'_{K'_a,K'_c} - J''_{K''_a,K''_c}$. The $C_3H_8 8_6 - 7_5$ line is a blend of eight ΔK_a, $\Delta K_c = 1$ transitions. Primary spectroscopic sources for molecular line frequencies: C_2H_3CN—Kisiel et al. (2009), C_3H_8—Drouin et al. (2006), HC_3N—Thorwirth et al. (2000), C_2H_5CN—Brauer et al. (2009), CH_3CN—Boucher et al. (1980).

performed using the `Clark clean` algorithm with a pixel size of 0.″025, a flux threshold of twice the expected rms noise, and a mask diameter of 1.″3 (8700 km at Titan's distance of 9.26 au), encircling the entirety of the detected flux from Titan's atmosphere.

The coordinate scales of the cleaned images were transformed to physical distances with respect to the center of Titan. Titan's north pole was oriented 5.°3 counterclockwise from celestial north, and tilted toward the observer by 26°. This is close to the maximum polar tilt due to the proximity of our observations to Titan's southern winter solstice on 2017 May 24.

3. *Cassini* Observations

Cassini's Composite Infrared Spectrometer (CIRS) is a Fourier transfer spectrometer covering 10–1500 cm^{-1} over three focal planes: FP1 (10–600 cm^{-1}), FP3 (600–1100 cm^{-1}), and FP4 (1100–1500 cm^{-1}). For additional details regarding the CIRS instrument, see Flasar et al. (2004) and Jennings et al. (2017). Here, we use data obtained using the FP3 and FP4 focal planes, which comprise linear arrays of 10 pixels each with a size of 0.27 mrad (Nixon et al. 2009b). These focal planes permit high spatial resolution nadir mapping of Titan's disk, as well as limb profiling of the atmosphere. The data presented here were obtained on orbits #261 (2017 February 17) and #275 (2017 May 24), the latter being *Cassini*'s final flyby of Titan on which whole-hemisphere CIRS (nadir) mapping was performed.

The CIRS nadir observations were taken with moderate (2.5 cm^{-1}) spectral resolution, which allowed rapid mapping of an entire hemisphere of Titan by scanning the FP3/4 pixel arrays in a "pushbroom" pointing sequence. Observations were obtained on orbit #275 at a distance of ~300,000 km from Titan, which resulted in a pixel size of ~100 km, or ~3° of latitude when projected to Titan's location. FP3 contained the prominent rovibrational emission bands of HCN, HC_3N, C_2H_2, C_2H_6, C_3H_4, and C_4H_2 in the range of 628–814 cm^{-1} (see Teanby et al. 2009 for example spectra). The interval 650–660 cm^{-1} is free from trace gas emission features and was used to determine the continuum level. In the present study, we focus primarily on the HCN and HC_3N data for comparison with ALMA observations of these species.

CIRS limb observations were obtained on orbits #261 and #275 with the FP3 and FP4 pixel arrays oriented perpendicular to the limb to give spectra covering tangent altitudes 0–600 km. Observations were in "sit-and-stare" mode at 0.5 cm^{-1} spectral resolution, resulting in high S/N, high-resolution spectra at a single latitude. Orbit #261 covered the latitude −11°(S) with a field-of-view size of ~45 km and #275 covered latitude −51° (S) with a field-of-view size of ~60 km. On orbit 261, only every other pixel was measured, so this observation had an equivalent vertical resolution of ~120 km.

4. Results and Analysis

4.1. Spectra and Maps

ALMA spectra for our main species of interest are shown in the left panels of Figures 1 and 2. These were obtained by integrating the reduced data cubes inside a circular aperture with radius 4300 km, centered on Titan (compared with the solid-body radius of 2575 km). This was sufficiently large to include all detected flux from the most extended (HNC) emission map. The resulting disk-integrated spectrum was too noisy to permit detection of C_2H_3CN, so the spectrum for this species was extracted from a beam centered at the emission peak for this molecule (200 km outside Titan's southern polar limb; see Figure 1).

Spectral features greater than 3σ above the noise were identified and integrated to produce the emission maps shown in the right panels of Figures 1 and 2. For C_2H_3CN, only three of the expected nine spectral lines were detected with greater than 3σ confidence (as shown in Table 1; two of these lines are blends of two closely spaced rotational transitions). The unexpected weakness of the C_2H_3CN emission could be explained by temporal variability with respect to the earlier studies of this molecule by Palmer et al. (2017) and Lai et al. (2017), but may also be due to relatively poor coupling between our ALMA beam and the intrinsic C_2H_3CN distribution—the earlier studies used a larger beam size (~1″), which was more sensitive to emission spread across Titan's entire ≈1″ disk plus atmosphere—whereas our ~0.″2 beam was only able to recover the compact C_2H_3CN emission peak near the south pole. To improve the S/N of the C_2H_3CN map in Figure 1, integration was performed over the frequency ranges corresponding to the nine expected strongest lines in one of our ALMA spectral windows (360.8–361.7 GHz), using the model of Palmer et al. (2017) as a guide for the line strengths, and adopting a 1.2 km s^{-1} integration width for each spectral line.

The resulting ALMA maps provide the highest-resolution (instantaneous) views of HNC, CH_3CN, C_2H_3CN, and C_2H_5CN in Titan's entire sunward-facing hemisphere published to date using any instrument. Characteristic emission patterns are apparent for each species, and provide, for the first time, a detailed view of the global column density distributions for these gases. Because most of the detected emission lines are relatively weak (and unsaturated), the majority of the observed molecular emission is expected to be optically thin (a notable exception is HC_3N, which becomes optically thick in the vicinity of the south pole; Cordiner et al. 2018). Titan's submillimeter continuum forms near the tropopause (at altitudes $z \approx 40$–60 km; Thelen et al. 2018), where the temperature T is close to 70 K. Our species of interest are synthesized primarily at higher altitudes (above a few hundred kilometers; e.g., Vuitton et al. 2019), where $T = 160$–180 K, and are subsequently transported to the lower stratosphere where they condense out (at $z \lesssim 90$ km; $T \lesssim 120$ K). Across Titan's disk (and limb), the targeted spectral lines are observed in emission because these gases are much warmer than the 70 K background continuum source of Titan (and the 2.73 K cosmic microwave background). Furthermore, while Titan's atmospheric temperatures are known to vary by up to ~±20 K with latitude (Achterberg et al. 2011), our observed lines are only weakly sensitive to temperature variations in this range (see, e.g., Lai et al. 2017; Thelen et al. 2019). These ALMA emission maps therefore provide a good indication of the intrinsic column density distribution of each species.

The HC_3N, CH_3CN, C_2H_3CN, C_2H_5CN, HCN, and HNC maps obtained using ALMA all show strong variations in column density across Titan's disk. Limb brightening dominates the HCN, HNC, and CH_3CN maps, characteristic of a relatively uniform latitudinal distribution, whereas the HC_3N, C_2H_3CN, and C_2H_5CN maps are dominated by polar emission, with the southern (winter) pole being strongest for the latter three species.

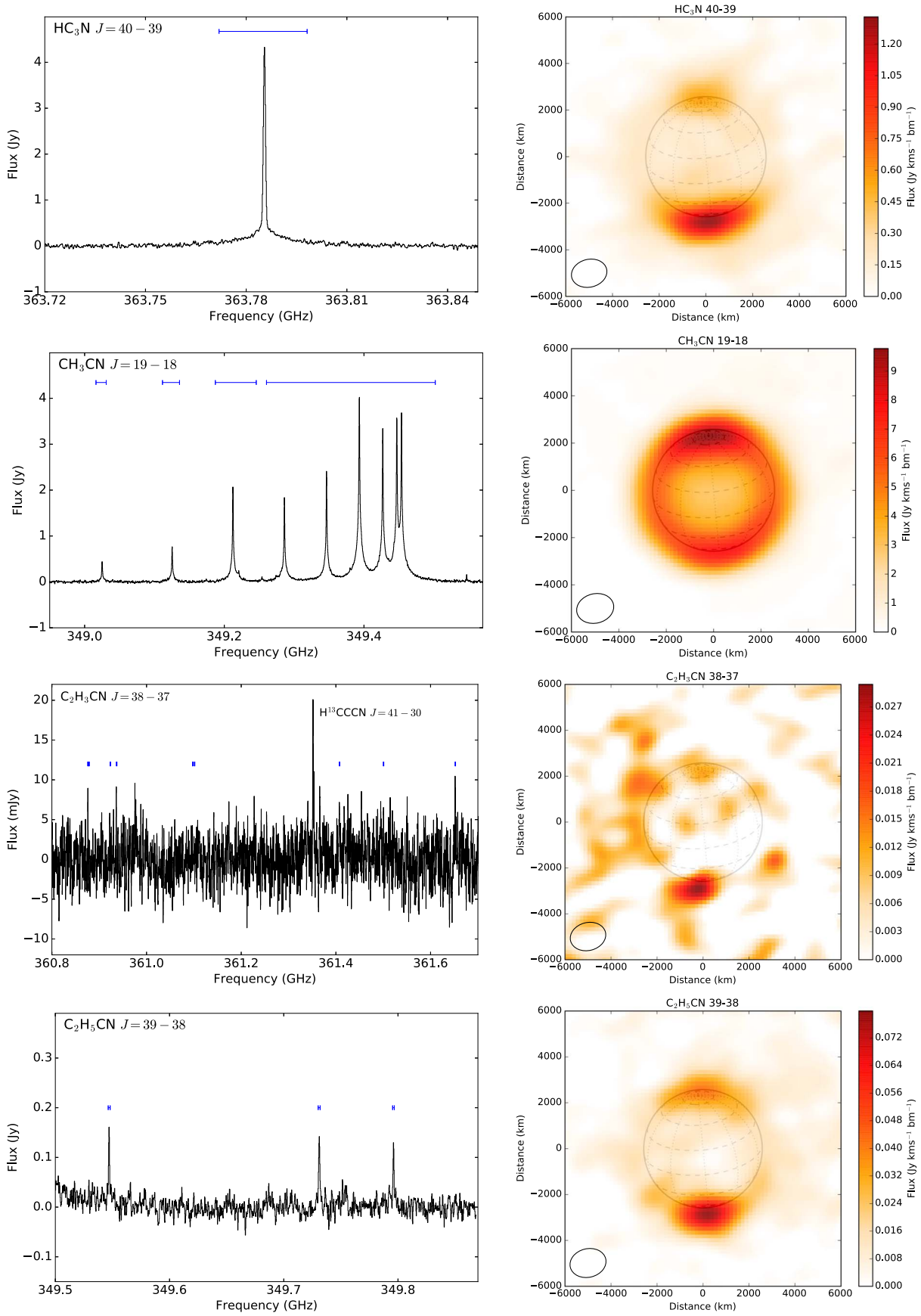

Figure 1. Continuum-subtracted molecular spectra and integrated emission maps for HC_3N, CH_3CN, C_2H_3CN and C_2H_5CN, observed using ALMA in 2017 May. Spectra (apart from C_2H_3CN) were integrated over a circular aperture with radius 4300 km, centered on Titan. The C_2H_3CN spectrum was extracted from a beam centered at the S-polar emission peak for that molecule. Spectral integration range(s) for the emission maps are shown with blue bars. The gray wireframe spheres indicate Titan's surface and alignment in the field of view. The ellipse (lower left) shows the spatial resolution (beam FWHM) for each map.

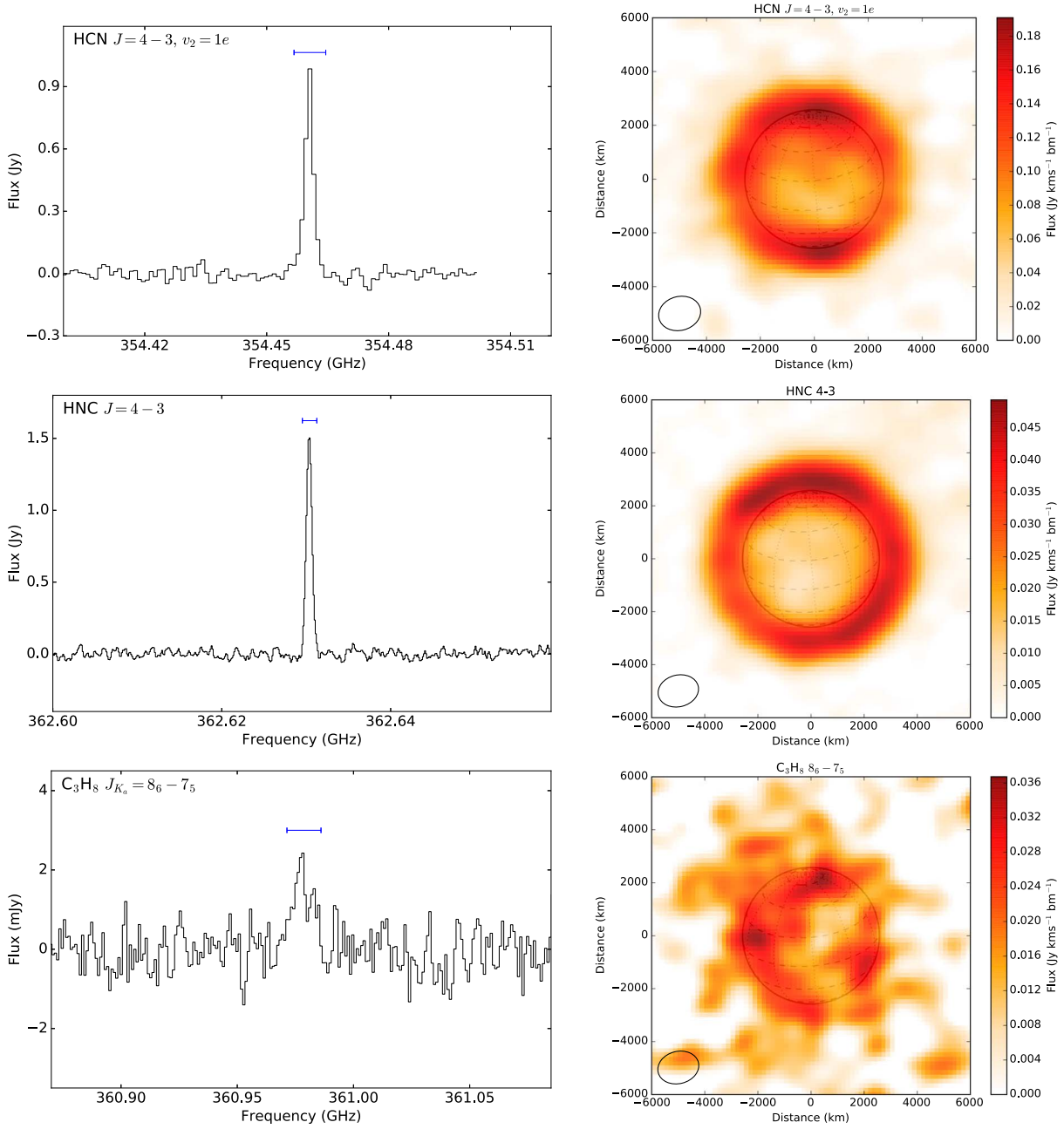

Figure 2. Same as Figure 1 but for HCN, HNC, and C_3H_8.

The HCN and HC_3N radiance maps obtained using *Cassini* CIRS (on orbit #275) are shown in Figure 3. While the spatial resolution is significantly better than obtained by ALMA, the basic morphology of the resulting maps is similar, with a dominant south polar emission peak for HC_3N (at latitudes $< -60°$) and a more uniform, limb-brightened distribution for HCN. The intensities of these vibronic emission bands observed by CIRS have a stronger dependence on temperature than the pure rotational transitions observed by ALMA. As a result, the relationship between CIRS-observed radiances and molecular column densities is nontrivial, making the interpretation of these maps more difficult. For example, it is likely that the drop in HCN radiance with decreasing latitude (south of the equator) is a consequence of falling stratospheric temperatures toward the winter pole (see, e.g., Teanby et al. 2017, 2019).

A unique aspect of our ALMA observations compared with typical (ground- or space-based) infrared measurements is the extremely high spectral resolution (up to $\nu/\Delta\nu \sim 10^6$), which enables the detection of emission lines from higher in the atmosphere ($z \gtrsim 200$ km). This is due to the relative lack of pressure broadening above ~200 km, resulting in the concentration of emission into narrow (thermally broadened) spectral line peaks. This benefit comes with the trade-off that we are less sensitive to low-altitude emission from the pressure-broadened line wings (below $\lesssim$200 km), although for the stronger lines (such as the pure rotational transitions of HC_3N and CH_3CN), we maintain good sensitivity down to the lower stratosphere (around 150 km; see, e.g., Thelen et al. 2019). While HCN and HC_3N have previously been extensively mapped at higher resolution by *Cassini* CIRS, instantaneous, whole-hemisphere limb coverage has not been possible at high

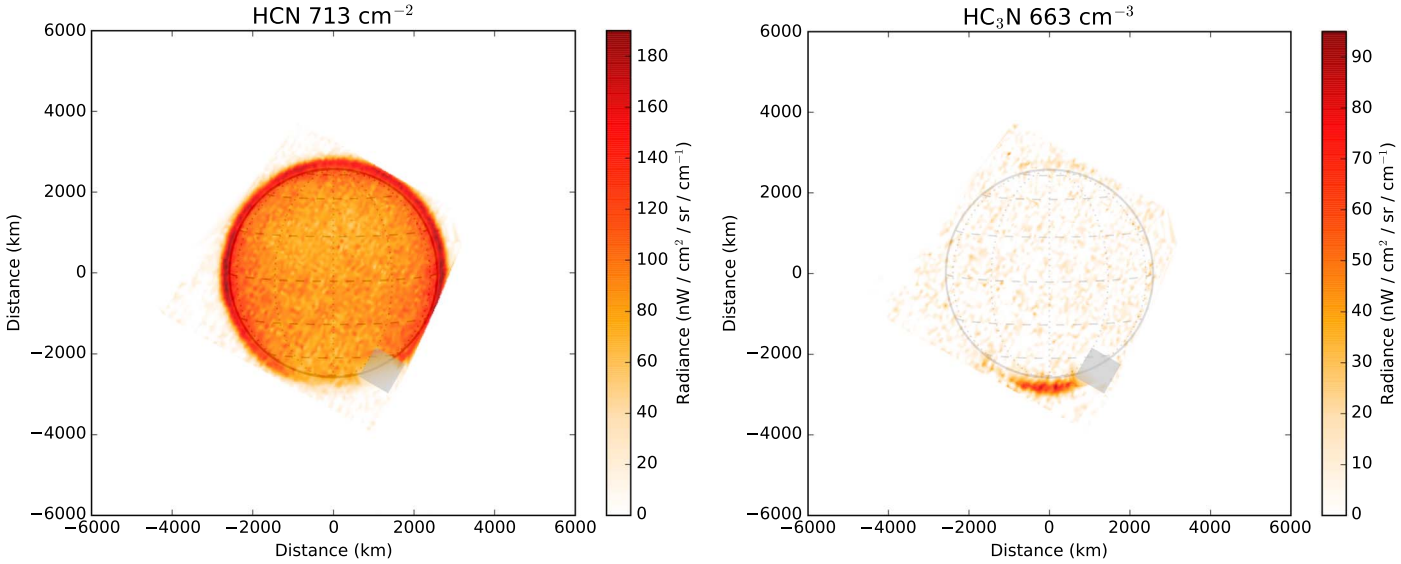

Figure 3. *Cassini* CIRS pushbroom maps of (continuum-subtracted) HCN and HC_3N emission from Titan, obtained during the 2017 May 24 flyby (*Cassini* orbit #275). Image frequencies are given for each molecule. Gray boxes indicate missing data.

resolution using that instrument; instead, CIRS limb maps may be built up by assembling data from multiple *Cassini* flybys over a period of months or years (during which time the atmosphere may have changed). Furthermore, CIRS nadir mapping is most sensitive to emission from altitudes around 150 km; our ALMA maps thus provide unprecedented spatial information at higher altitudes, for the 2017 May (solstice) epoch.

While the main focus of our present study is on the nitrile observations, we also obtained a serendipitous detection of the C_3H_8 $J_{K_a} = 8_6 - 7_5$ multiplet at 360.978 GHz (comprising a blend of eight transitions with $\Delta K_c = 1$). This is the first time propane has been definitively detected and mapped in any extraterrestrial source at radio wavelengths (following a tentative ALMA detection on Titan by Lai et al. 2017), and is therefore worthy of further investigation. While C_3H_8 has an extremely weak radio spectrum due to its small dipole moment and large partition function, the large abundance of this molecule in Titan's atmosphere enables its detection using ALMA. Vibrational emission from C_3H_8 was previously detected on Titan by *Voyager* 1 (Maguire et al. 1981), the *Infrared Space Observatory* (Coustenis et al. 2003), and *Cassini* (Nixon et al. 2009a). Our ALMA map shows a relatively uniform distribution for C_3H_8 across Titan's disk, with little evidence for any latitudinal variability above the (admittedly high) noise level.

Maps and spectra of the HC_3N vibrationally excited lines and isotopologues have already been presented by Cordiner et al. (2018), and are consistent with the overall distribution of the HC_3N $J = 40$–39 line in Figure 1, but provide a more accurate representation of the HC_3N column density distribution (albeit at lower S/N), due to their reduced optical depth (see Section 4.2). We also obtained high-sensitivity CO and HCN spectra (including the main $J = 4$–3 line of HCN as well as its ^{13}C and ^{15}N isotopologues). Unfortunately, these lines were too optically thick to provide useful emission maps and require detailed radiative transfer modeling for their analysis, which will be presented in a future article. We use the vibrationally excited HCN ($J = 4$–3, $v_2 = 1e$) line as an alternative to mapping the ground-state ($J = 4$–3) line of this molecule, the core of which is completely optically thick (self-absorbed) across much of Titan's disk. The HCN $v_2 = 1e$ line is predominantly optically thin, but sits atop the strong, pressure-broadened wing of the $J = 4$–3 (ground state) HCN line wing, which was subtracted using a polynomial fit, thus allowing the $v_2 = 1e$ line to be mapped.

4.2. Latitudinal Profiles

The latitudinal variability observed in Figures 1 and 2 can be quantified by plotting the flux as a function of (sky-projected) angle about Titan's disk center. To eliminate the impact of the differing (elliptical) beam dimensions as a function of angle, it was first necessary to degrade the resolution of our images so as to produce a circular point-spread function (with diameter equal to that of the long axis of the original beam ellipse). The average flux was then obtained for each species inside radial wedges (of angular size ϕ_w), originating from the center of Titan's disk, and plotted as a function of angle from the perpendicular bisector of Titan's polar axis in Figure 4. A wedge size $\phi_w = 10°$ was used for all molecules apart from C_2H_3CN and C_3H_8, for which 30° was used, to improve the S/N for these species. The angular coordinate system and binning scheme are shown in the top-right panel for CH_3CN. The relationship between the angular range covered by each wedge and the corresponding latitude on Titan is complicated due to the finite wedge size and the tilt of Titan's pole. This results in complete obscuration of the south polar region, while at the north pole, a relatively large range of latitudes is included in each wedge. The weighted-mean latitude was taken within each wedge, using tangent latitudes for pixels falling outside Titan's limb. These weighted-mean latitudes are shown on the upper abscissa axes in Figure 4.

The isomeric partners HNC and HCN are shown on the same plot (with HNC multiplied by a factor of 5 for display). The profile for vibrationally excited HC_3N ($v_7 = 1$) is shown in addition to the ground-state ($v = 0$) transition for that molecule (multiplied by 3 for display). Cordiner et al. (2018) determined that the ground-state HC_3N rotational lines in ALMA Band 7 become highly saturated at the south pole, which makes the $J = 40$–39, $v = 0$ transition unreliable as a measure of the

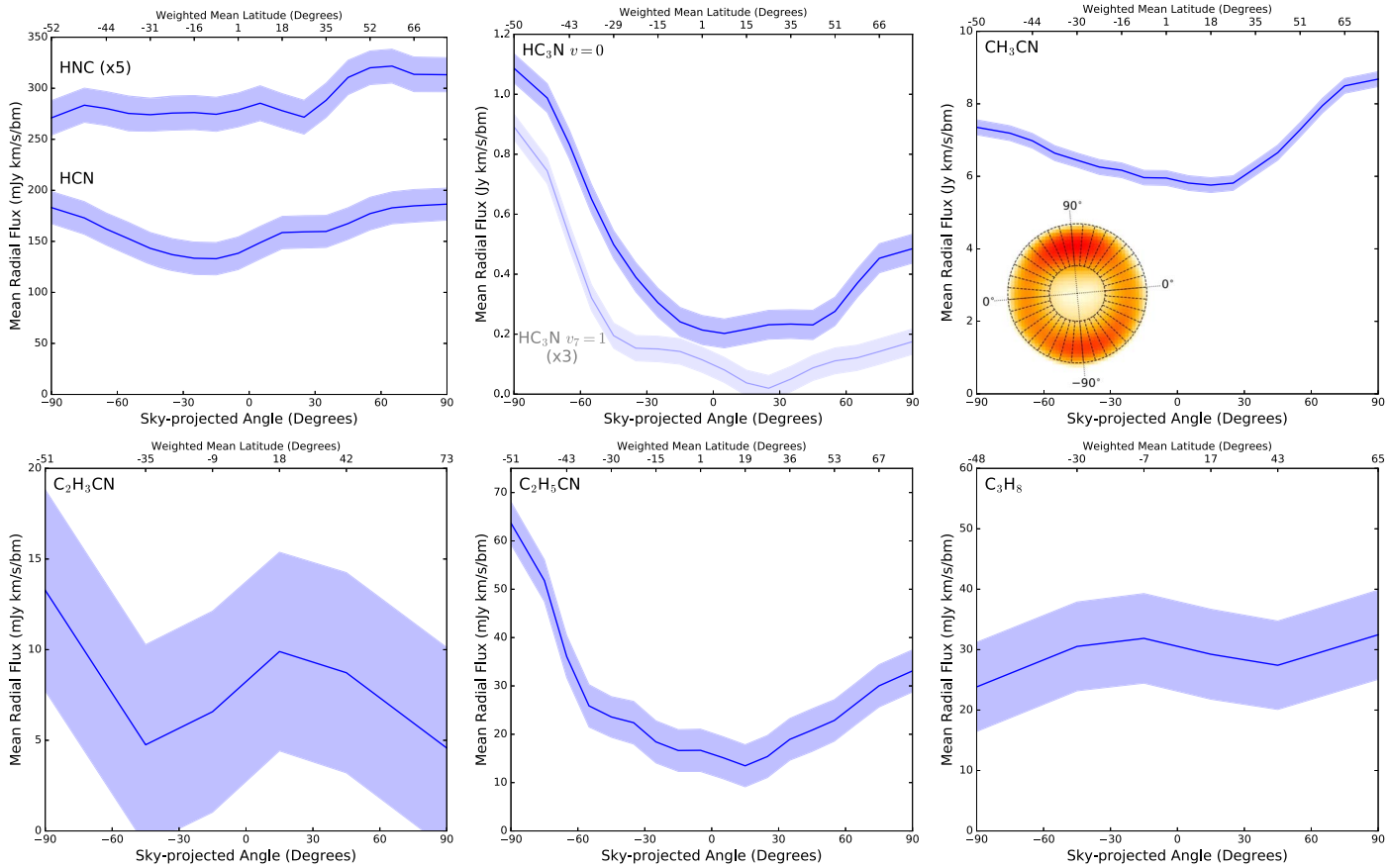

Figure 4. ALMA fluxes (radially averaged) as a function of angle from the bisector of Titan's sky-projected polar axis—the coordinate system and angular binning scheme are indicated by the inset in the upper-right panel. Blue envelopes show the $\pm 1\sigma$ error range. The weighted-mean latitudes for each measurement are shown on the upper abscissa axes. HCN and HNC are shown in the same panel for comparison (with the HNC profile multiplied by 5 for display); similarly, the HC_3N $v_7 = 1$ profile is shown in a lighter color (multiplied by a factor of 3), for comparison with HC_3N $v = 0$.

HC_3N column density at that location. The $v_7 = 1$ transition, by contrast, is reasonably optically thin and thus provides an improved measure of the true HC_3N distribution.

Significant latitudinal variations are apparent for HCN, HC_3N, CH_3CN, and C_2H_5CN. The strongest variations are for HC_3N and C_2H_5CN, which peak in the vicinity of the south pole and fall sharply toward the equator (over a distance smaller than the spatial resolution element). This behavior is consistent with high concentrations of these gases within regions $\lesssim$500 km from the pole. HC_3N and C_2H_5CN show a weaker peak over the north pole. By contrast, CH_3CN peaks most strongly in the north, whereas the HCN northern and southern abundance peaks are of similar strength. C_3H_8 shows no evidence for significant latitudinal variation.

4.3. Longitudinal Variability of HNC

The only species to show significant longitudinal (east–west) variability is HNC, manifested by a relative weakness in the HNC emission on the western (dawn) limb. Figure 5 (top panel) shows the average flux (in 30° radial wedges), as a function of angle (ϕ) about the disk center, measured from the sky-projected north polar axis. The HNC emission is strongest at the north pole, relatively uniform in the eastern hemisphere, then begins to fall toward the south pole (from around $\phi = 150°$), reaching a trough in the west ($\phi = 250°$), before rising back to the northern peak. The longitudinal asymmetry of HNC is demonstrated more clearly in the bottom panel of Figure 5, where the east–west flux difference (S(east–west)) is plotted as a function of angle from the bisector of Titan's sky-projected polar axis. Corresponding weighted-mean latitudes (shown on the upper abscissa) were calculated as in Section 4.2. The east–west flux difference is seen to reach a peak close to (or slightly south of) the equator. The southerly bias could be a result of viewing geometry, due to the tilt of Titan's polar axis.

Such longitudinal asymmetry is surprising given the presence of fast, superrotating zonal winds (Lellouch et al. 2019), which traverse Titan's globe in a period of less than a few Earth days, and are therefore expected to quickly even out atmospheric inhomogeneities as a function of longitude. While Cordiner et al. (2014) claimed the first evidence for longitudinal variations in Titan's HNC, their measurements were from relatively low-resolution, low-sensitivity flux calibration data, and the observed east–west asymmetries could plausibly have resulted from the combined effects of noise and smearing by a strongly elliptical telescope beam (M. Gurwell 2016, private communication). The HNC asymmetries presented here are clearer and more robust than those identified by Cordiner et al. (2014). We measure a total HNC flux of $S_E = 383 \pm 7$ mJy km s^{-1} from Titan's eastern hemisphere and $S_W = 338 \pm 7$ mJy km s^{-1} from the western hemisphere, which amounts to a ratio $S_E/S_W = 13\% \pm 3\%$. Thus, a conclusive 4.3σ difference is identified in the HNC flux between the hemispheres. Use of a circularized beam renders this result free from any geometrical artifacts related to (elliptical) beam smearing.

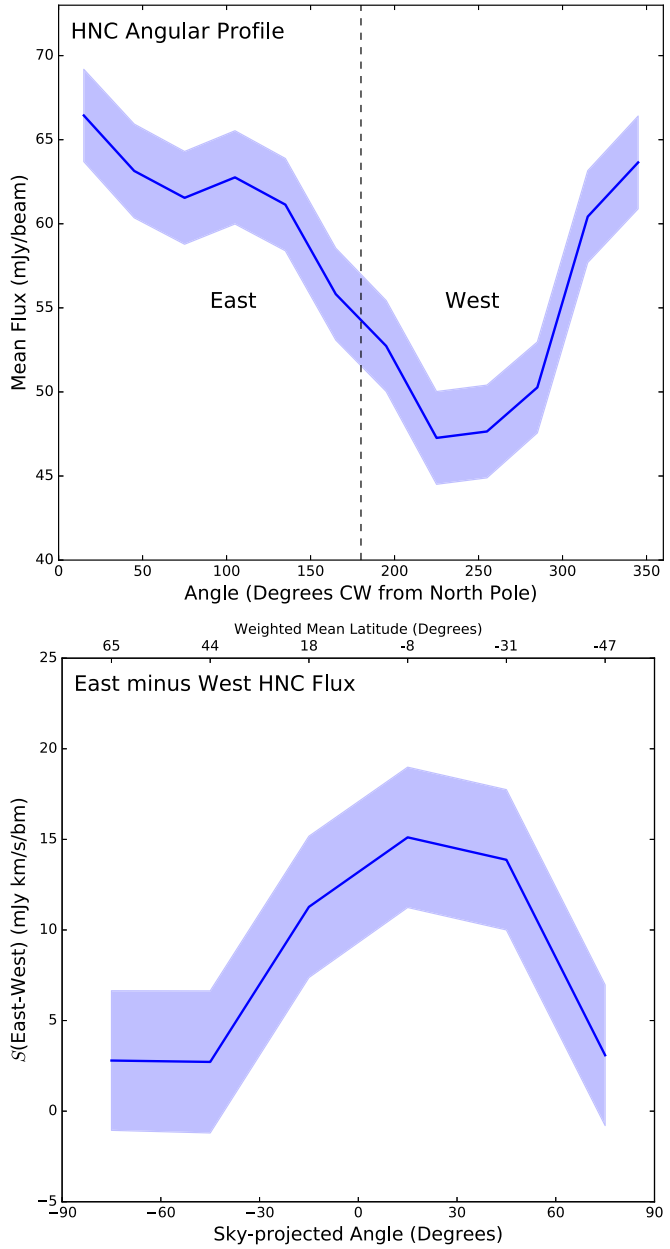

Figure 5. Top: average radial HNC flux as a function of angle from Titan's sky-projected north polar axis. Dashed line indicates 180° (i.e., the south pole). Bottom: flux difference (east minus west) for HNC, as a function of angle from the bisector of Titan's sky-projected polar axis, demonstrating a clear east–west asymmetry.

4.4. ALMA Limb Abundance Retrievals

The variation in integrated line flux (S) as a function of sky-projected radial distance from Titan's limb (r) contains information on how the gas density (x) varies as a function of altitude (z). The vertical abundance profile $x(z)$ can thus be retrieved for each gas by fitting an atmospheric model to the ALMA observations. Despite coarse radial sampling due to limited angular resolution, our $S(r)$ measurements can nevertheless provide unique information on the high-altitude abundances for our species of interest. To generate $S(r)$ at the highest resolution (at the expense of some sensitivity), Briggs weighting of the interferometric data was used (with a *robust* parameter of zero), leading to a resolution of $0.15 \times 0.''13$ (≈900 km) at 362 GHz.

We generated $S(r)$ profiles by remapping the image pixels onto a polar grid with origin at the center of Titan's disk. Fluxes as a function of radius were extracted and averaged within angular regions $\phi = 45°$–$135°$ and $\phi = 225°$–$315°$. These ranges were chosen in order to capture a sufficiently large range of equatorial latitudes for maximum S/N while excluding the more complex polar regions (seen for HC_3N, CH_3CN, C_2H_3CN, and C_2H_5CN in Figure 1). Abundance enhancements at the winter pole are associated with subsidence within a highly localized region inside Titan's polar vortex (Teanby et al. 2008, 2017; Vinatier et al. 2015). This leads to the downwelling of photochemically enriched gases, resulting in a distinctly different abundance (and temperature) profile at the winter pole compared with equatorial regions. Our simplistic, 1D modeling procedure provides an estimate of the mean abundance profile at equatorial latitudes (where the abundances are dominated by high-altitude chemistry), to the exclusion of the polar regions, which are strongly influenced by seasonally variable gas dynamics.

The peak-normalized $S(r)$ profiles are shown in Figure 6 (top panel). Clear separations are present between the peak emission radii (r_p) for each species, which were derived from the centroids of the $S(r)$ profiles, and are given in Table 2. While the C_3H_8 and CH_3CN fluxes peak at $r_p = 2400$ km and 2590 km, respectively (close to the edge of Titan's solid $r = 2575$ km disk), C_2H_5CN, HCN, HC_3N, and HNC peak well outside this radius, indicating flux contributions from high altitudes—the very high HNC peak emission radius of 3140 km is particularly surprising and is consistent with a dominant thermospheric/ionospheric flux contribution for this gas. Unfortunately, an $S(r)$ profile (and corresponding r_p value) could not be generated for C_2H_3CN due to a lack of flux from this molecule near the equator.

To further interpret the observed limb profiles, it is necessary to account for the line-of-sight averaging of different altitudes within each ALMA beam, as well as the atmospheric density (and temperature) variation with altitude. This was done by constructing a simple, spherically symmetric molecular emission model for Titan. The density profile was taken from Krasnopolsky (2009), and temperatures were retrieved from CIRS CH_4 limb observations at −27° latitude (observed during rev#275), using the method of Teanby et al. (2007). Molecular abundances as a function of altitude ($x(z)$) followed the simplest polygonal scheme possible while preserving a good fit to the observations: a logarithmic abundance gradient was adopted between altitudes z_1 and z_2, with zero abundance below z_1 and constant abundance above z_2. Spectral line fluxes were generated using parameters from the Cologne Database for Molecular Spectroscopy (Müller et al. 2001), under the assumption of optically thin emission. To reproduce the ALMA spatial response, the resulting images were passed through the ALMA simulator (using the `Simobserve` and `Clean` tasks), with the same observational and imaging parameters as described in Section 2. Synthetic image cubes were integrated over the same spectral ranges as the observations (Figures 1 and 2), and radial flux profiles were extracted for comparison with observation.

The best-fitting z_1, z_2, and abundance gradient parameters were obtained through nonlinear least-squares optimization using the MPFIT routine (Markwardt 2012), and 1σ parameter errors were determined from the covariance matrix. The corresponding optimized limb flux models are shown for comparison with observations in the Appendix (Figure 9), and retrieved abundance

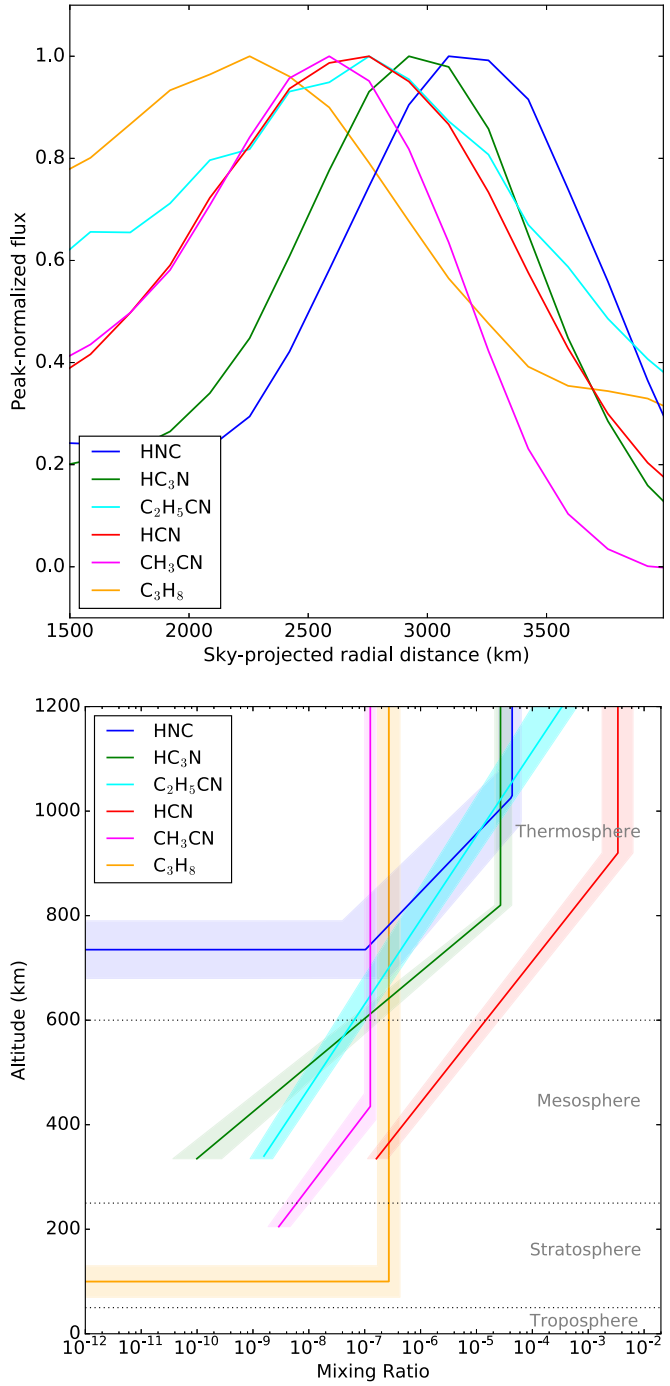

Figure 6. Top panel: peak-normalized equatorial limb flux profiles observed using ALMA (excluding the regions within ±45° of Titan's north and south poles). Distances are with respect to the center of Titan's disk, projected in the plane of the sky. Bottom panel: retrieved vertical abundance profiles with 1σ error envelopes.

profiles are shown in Figure 6 (lower panel). Given the simplicity of our abundance parameterization scheme, the model limb flux profiles provide a surprisingly good fit for all species, with respect to the observational 1σ noise errors.

To determine the altitude sensitivity of our abundance models, contribution functions (total flux as a function of altitude) were calculated within an ALMA beam centered on the respective r_p value for each species. The retrieved abundances are considered to be most reliable around the

Table 2
Peak ALMA Limb Emission Radii (r_p), Weighted-mean Contribution Function Altitudes ($\bar{z}_{CF}$), and Modeled Lifetimes at 300 km (L_{300})

Species	r_p (km)	$\bar{z}_{CF}$ (km)	L_{300} (yr)[a]
HCN	2670	530	350
HNC	3140	970	0.6
HC_3N	2930	760	2.6
C_2H_3CN	…	…	1.0
C_2H_5CN	2670	610	3.2[b]
CH_3CN	2590	270	91
C_3H_8	2400	130	13

Notes.
[a] Lifetimes (L_{300}) are the chemical/dynamical lifetimes at 300 km from Vuitton et al. (2019).
[b] The lifetime for C_2H_5CN is from a model including loss via sticking to aerosols.

flux-weighted mean altitude ($\bar{z}_{CF}$) of the contribution function, and these values are given in Table 2. Pressure-broadened line wings become significant in models for HC_3N and C_2H_5CN submillimeter emission at altitudes below ~300 km (Cordiner et al. 2015; Thelen et al. 2019), but such line wings are absent (or below the noise threshold) in our ALMA limb spectra, so the retrievals for these molecules contain little useful information below this altitude. We therefore truncate the abundance profiles for these species below 300 km in Figure 6. We also truncate the HCN profile below 300 km due to the difficulty in reliably separating the wings of the $v_2 = 1e$ line from those of the ground-state HCN ($J = 4$–3) line. This region of the HCN ($J = 4$–3) line wing originates predominantly from altitudes 100–200 km (Molter et al. 2016) and is strong enough to call into question the validity of the optically thin approximation for this molecule, which may therefore have also resulted in underestimating the overall HCN abundances. By virtue of its intrinsic line strength and high abundance at lower altitudes, pressure-broadened wings were clearly detected for CH_3CN, allowing the abundance for this species to be retrieved down to $z \sim 200$ km (determined using the CH_3CN contribution function of Thelen et al. 2019).

Our ALMA limb observations provide the first well-constrained abundance retrievals for HNC and C_2H_5CN in the upper atmosphere. Prior (disk-averaged) observations of these molecules by Moreno et al. (2011) and Cordiner et al. (2015) were only able to place lower limits (of 400 km and 200 km, respectively) on the altitudes from which the emission from these species originated. Our limb profile modeling shows that the detected HNC emission is confined to thermospheric altitudes above 730 ± 60 km, whereas C_2H_5CN follows a steep (logarithmic) abundance gradient from $(1.4 \pm 0.7) \times 10^{-9}$ at 340 km to $(4 \pm 3) \times 10^{-4}$ at 1200 km. While the present article was undergoing peer review, the study of Lellouch et al. (2019) was published, also confirming that HNC is restricted to the thermosphere.

5. Comparison with *Cassini* CIRS

Accounting for variations in atmospheric temperature and instrumental resolution, the primary morphology for HCN and HC_3N observed by CIRS is consistent with that revealed by our ALMA observations. Both *Cassini* and ALMA reveal that most of the HCN emission is concentrated in an atmospheric band (relatively uniform with latitude), at altitudes between 50–400 km. The HC_3N emission is dominated by a higher-altitude, southern

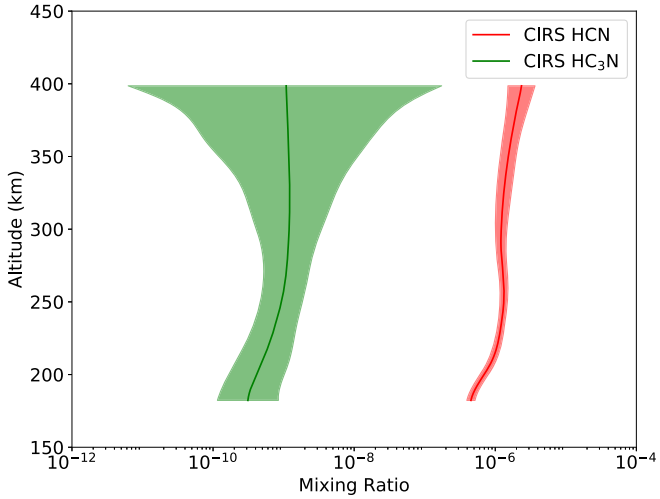

Figure 7. *Cassini* CIRS limb abundances for HCN and HC_3N, retrieved at latitude $-11°$.

polar peak, confined to latitudes south of $-60°$. The northern HC_3N peak detected by ALMA is barely visible in the *Cassini* nadir observations, which is consistent with the north-to-south column density ratio of $\approx 1/7$ determined from the ALMA $v_7 = 1$ lines. As explained in Section 4.1, CIRS HCN radiances have a significant temperature dependency, which can explain the lack of a southern polar emission peak—in fact, the CIRS HCN flux reaches a minimum at the south pole, where the ALMA flux reaches a maximum.

To enable a more direct comparison of the ALMA and *Cassini* observations, vertical profiles of the temperature, and HCN and HC_3N abundance were retrieved from the CIRS data by modeling the limb radiances. The NEMESIS spectral inversion tool (Irwin et al. 2008) was used to fit the $-11°$ limb observations from orbit #261, following the method of Teanby et al. (2007). Prior to inverting for composition, a cubic b-spline curve was fitted to the measured radiance profiles at each wavenumber using a knot spacing of 100 km (see Teanby 2007 for further details). This improved the S/N by smoothing the radiance through multiple pixel measurements at similar but not identical tangent altitudes. The profiles obtained are reliable for 180–400 km; below 180 km, the line opacity was too high to allow an accurate determination, and above 400 km the signal-to-noise ratio (S/N) was too low.

Retrieved equatorial limb abundances for HCN and HC_3N are shown in Figure 7. By comparison with Figure 6, these are seen to be in reasonable agreement with the ALMA limb abundance profiles, especially when considering the error bars on the ALMA and CIRS retrievals, as well as the (unquantified) uncertainties in the ALMA limb abundances due to the low spatial resolution and simplified (polygonal) parameterization scheme used for those data.

6. Discussion

6.1. Chemistry and Dynamics of the Thermosphere/Ionosphere Probed by HNC

Our HNC observations reveal that this molecule is confined predominantly to the thermosphere, with an abundance of $(4.3 \pm 1.3) \times 10^{-5}$ above 1030 km. The retrieved abundance profile (Figure 6) is remarkably similar to the photochemical model results of Vuitton et al. (2019; shown in Figure 8). The

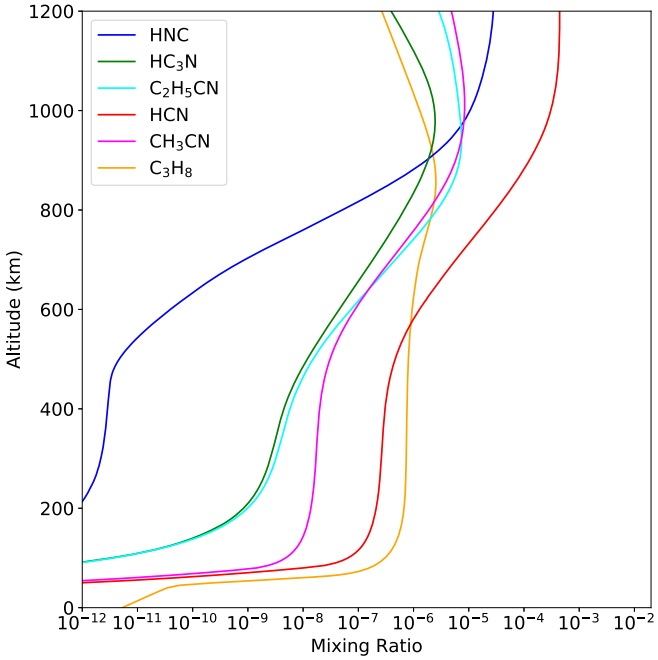

Figure 8. Predicted equatorial abundances as a function of altitude, from the recent photochemical model of Vuitton et al. (2019). The C_2H_5CN and HC_3N models include loss via sticking to aerosols.

HNC model abundance profile rises steeply in the range 600–1000 km and reaches a peak abundance $\sim 2 \times 10^{-5}$ in the range 1050–1100 km. The very good agreement between model and observation for this species provides a strong validation for the chemical reaction scheme of Vuitton et al. (2019), in which HNC is produced by electron recombination of the abundant $HCNH^+$ ion and is rapidly converted back to the lower-energy HCN isomer (on a timescale of about a day), primarily by collisions with ionospheric H atoms. The short chemical lifetime means that HNC is destroyed before it can diffuse down through the atmosphere from its high-altitude production site and is therefore confined to the thermosphere, with negligible abundance at lower altitudes. The rapid destruction of HNC makes it a potentially unique probe of very short-timescale dynamical processes in Titan's upper atmosphere.

The observed asymmetry in HNC emission between Titan's eastern and western hemispheres can be explained as a result of the combined effects of photochemistry and atmospheric dynamics. The presence of mesospheric zonal winds (in the altitude range 250–450 km) was initially inferred on Titan based on the atmospheric structure derived from stellar occultation observations by Hubbard et al. (1993). High-altitude (450–1000 km) superrotating winds were subsequently detected by Moreno et al. (2005) using ground-based interferometry. Cui et al. (2009) measured a strong (order of magnitude) diurnal variation in Titan's ionospheric $HCNH^+$ abundance using *Cassini* mass spectrometry, with the ion strongly depleted in the night hemisphere. They constructed a chemical/dynamical model for the ionosphere, which showed that east–west asymmetry in the distribution of $HCNH^+$ (and other ions) can be produced by a zonal wind that sweeps ion-rich material from the day side toward the eastern (dusk) terminator. The rapid conversion of $HCNH^+$ to HNC via electron recombination would then lead to enhanced HNC abundance at the eastern limb. As it passes across the night

side, collisional isomerization converts HNC back to HCN, resulting in the subsequent emergence of HNC-depleted air in the west. The detection by Lellouch et al. (2019) of superrotating zonal HNC winds extending up to the ionosphere lends support to this theory, so in situ production of an asymmetric $HCNH^+$ distribution by electrons from Saturn's magnetosphere (e.g., Cravens et al. 2009) may not be required.

The HNC $J = 4$–3 line flux has a relatively weak dependence on temperature, so a relatively large, 30–40 K hemispheric difference in rotational temperature would be required to explain the observed asymmetry. The atmospheric circulation model of Müller-Wodarg et al. (2000) predicted a diurnal temperature variation of 10–20 K (the precise value depends on solar activity), at an altitude of 1300 km, corresponding to the top of Titan's thermosphere. However, this variation was found to fall with decreasing altitude, becoming negligible at the ~970 km altitude to which our HNC observations are most sensitive. Combined with the relatively low solar activity around the time of our observations, diurnal temperature variations seem an unlikely explanation for the observed HNC asymmetry.

6.2. High-altitude Nitrile Chemistry

6.2.1. Inferred Molecular Lifetimes

The vertical abundance profiles retrieved for the remaining nitriles (HCN, CH_3CN, HC_3N, and C_2H_5CN) are broadly consistent (within about an order of magnitude) with the results of recent chemical models (e.g., Krasnopolsky 2009; Loison et al. 2015; Dobrijevic et al. 2016; Willacy et al. 2016; Vuitton et al. 2019), confirming the efficient production of organics through photochemistry in the thermosphere (above 600 km), initiated by solar ultraviolet radiation. An abundance gradient develops as photochemical products mix downward toward the lower stratosphere, where the temperature becomes low enough for them to precipitate out. The steepness of the abundance gradient is affected by the chemical lifetime of each species, so from Figure 6, we may infer that after HNC, HC_3N has the next shortest lifetime, followed by HCN, C_2H_5CN, then CH_3CN. The overall trend is compatible with the lifetimes predicted at 300 km by Vuitton et al. (2019) (see Table 2), although it should be noted that their base model overestimated the stratospheric C_2H_5CN abundance, so the lifetime for this species is taken from their alternative model where C_2H_5CN is lost from the gas phase via sticking to stratospheric aerosol particles. The steep abundance profile for HCN also seems to be inconsistent with a long (350 yr) lifetime at 300 km. However, the HCN model lifetime varies strongly with altitude and takes a value of only about a few years in the lower thermosphere.

As a result of the coupling between the observed gas spatial distributions and Titan's seasonally varying global circulation, approximate lifetimes may also be derived from our ALMA emission maps, based on the rate of decay of abundance at the summer pole since the time of the last seasonal reversal. We begin with the assumption that sufficient time has elapsed since the last seasonal reversal (following the 2009 equinox) so that the molecular abundances at the southern (winter) pole are in a quasi-steady state, maintained by a balance between the source (Titan's global meridional circulation system) and sink (photochemical destruction). Then, ignoring temperature effects (which are expected to have only a small impact on the measured fluxes; see Section 4.1), the peak of the spectrally integrated flux in the southern hemisphere (F_S) for a given species at the present epoch is taken to be representative of the peak flux that would have been present in the north at the time of the last circulation reversal. This is supported by Teanby et al. (2019), who suggested that north and south polar stratospheric abundances are closely comparable at similar seasonal phases, based on trends observed in CIRS nadir data across the entire *Cassini* mission. Using temporally resolved molecular observations from CIRS, Vinatier et al. (2015) determined that the last circulation reversal occurred in 2011, so that the peak north polar flux (F_N) has decayed to reach its present value over a period of 6 yr.

Assuming exponential decay of the form $dF_N/dt = F_S e^{-t/\tau}$, the following lifetimes τ were derived—HC_3N: 3.4 yr, C_2H_3CN: <11.3 yr, C_2H_5CN: 9.3 yr. These values are in reasonable agreement with the chemical/dynamical lifetimes (L_{300}) from the model of Vuitton et al. (2019; see Table 2). We measure $F_N > F_S$ for CH_3CN, which implies that the south polar abundance for this species has not yet reached steady state, so its lifetime cannot be derived using our method. However, the fact that the north and south polar fluxes differ indicates that the lifetime for this species is probably less than (or similar to) the 29.5 yr Saturnian year; if it were much longer, $F_N \approx F_S$ would be expected as a result of the repeated replenishment of chemically enriched polar gases following successive winters. For HCN, we find $F_N \approx F_S$, which implies a relatively long lifetime for the observed (polar) gases, consistent with the larger values of 60 yr and 350 yr at 300 km calculated by Dobrijevic et al. (2016) and Vuitton et al. (2019), respectively.

These τ values represent an average measure of the molecular lifetime due to the combined influx/loss rates of molecules to/from the north polar region as a result of photolysis, chemical reactions, precipitation, diffusion, advection, and winds, and may therefore not be considered as directly comparable with values from one-dimensional chemical models. Additional caution is required for their interpretation, due to the gross assumptions made in their derivation. In particular, the south polar flux at the present epoch may not be precisely representative of the northern value at the time of the 2011 circulation reversal, which may be the case if steady state was not reached in time, or in the case of seasonal climate asymmetry (i.e., if the atmosphere in Titan's northern winter is not a mirror image of the southern winter). Furthermore, the 27° tilt of Titan's polar axis means that the south polar region was partially obscured from view at the time of our observations, so that F_S provides an underestimate of the total flux. However, the majority of our observed flux is from altitudes above 200 km and latitudes $>-80°$, all of which are within view, so geometrical obscuration is not expected to be a dominant source of uncertainty.

6.2.2. Comparisons with Prior Observations and Models

Our ALMA limb abundance profiles for HCN, HC_3N, and CH_3CN are in general closely consistent with the prior equatorial retrievals from Thelen et al. (2019), obtained by modeling ALMA spectra at lower spatial resolution. Our C_2H_5CN profile between 300 and 600 km is quite consistent with the disk-averaged gradient profile from Cordiner et al. (2015). The thermospheric HCN profile also matches reasonably well with the *Cassini* VIMS limb observations of Adriani et al. (2011). It should be noted that the vertical abundance retrievals in our present study (based on spectrally integrated

limb fluxes) contain only limited information due to the relatively coarse (>900 km) spatial resolution of our data, and correspondingly simplified (polygonal) parameterization scheme for the abundances as a function of altitude. As such, our ALMA retrievals should be considered only approximate; full retrievals taking into account the detailed (pressure-broadened) spectral line profiles will be presented in a future article. Nevertheless, some useful comparisons between our results and prior observations and models can still be made, particularly at higher altitudes (above 500 km) where previous (IR and radio) retrievals contain little useful information.

The retrieved HCN, HNC, HC_3N, C_2H_5CN, and C_3H_8 abundances at an altitude of 1000 km are close (within errors) to those predicted by the models of Loison et al. (2015), Willacy et al. (2016), and Vuitton et al. (2019). Predicted vertical abundance profiles from Vuitton et al. (2019) are shown for comparison with our observations in Figure 8. For CH_3CN, these models overestimate the ionospheric abundance by about an order of magnitude, which may indicate the presence of unaccounted-for (or underestimated) destruction pathway(s) for this molecule. It should be noted that although our HCN profile matches the model of Vuitton et al. (2019) reasonably well in the mesosphere and above, our retrieved HCN abundances are more uncertain toward lower altitudes, due to the difficulty in separating the wings of the $J = 4$–3, $v_2 = 1e$ line from those of the main ($J = 4$–3) line.

ALMA equatorial limb data show that HC_3N maintains a high abundance to lower altitudes than predicted by the Loison et al. (2015) and Dobrijevic et al. (2016) models, which fall too rapidly in the lower thermosphere (between 800 and 600 km). The models of Willacy et al. (2016) and Vuitton et al. (2019) provide a better overall match for our HC_3N observations. Note, however, that there is still some considerable uncertainty regarding the rate of loss of HC_3N via sticking to aerosol particles in the Vuitton et al. (2019) model, so additional studies are needed to fully understand the chemistry of this species.

In summary, the reasonably good agreement between our nitrile observations and photochemical models for Titan's mesosphere and thermosphere indicates that the fundamental processes involved in the high-altitude production of nitriles are quite well understood. However, toward the stratosphere, the base model of Vuitton et al. (2019) does a relatively poorer job of matching the HC_3N and C_2H_5CN observational data, which are overpredicted by at least an order of magnitude (a similar problem occurs in the lower stratosphere for the Loison et al. 2015 and Dobrijevic et al. 2016 models), indicating that important loss mechanisms for these molecules may be missing from chemical networks. This issue may be addressed with the inclusion of sticking of these molecules to aerosol particles as an additional loss process in the stratosphere.

7. Conclusions

The ALMA observations presented here constitute a comprehensive, moderate-resolution mapping of Titan's most abundant atmospheric nitriles around the time of the 2017 solstice, coinciding with the end of the *Cassini* mission. This is the first time detailed, whole-hemisphere maps have been published for the complete set of nitriles accessible in the microwave/submillimeter band and constitutes a unique resource for investigating their global distributions. Each species shows a characteristic spatial distribution, resulting from the interplay between photochemical production, destruction, and atmospheric dynamics. ALMA's unique capability to probe narrow molecular emission lines from high altitudes (~300–1000 km) in the mesosphere and thermosphere, in addition to pressure-broadened emission from lower, stratospheric altitudes (~70–300 km) provides complementary data to those obtainable using infrared instruments such as *Cassini* CIRS and IRTF TEXES.

Our global maps for HC_3N, C_2H_3CN, and C_2H_5CN reveal strong, compact emission peaks over the southern (winter) pole, indicative of rapid photochemical production (and destruction) at high altitudes, combined with transport toward southern latitudes by Titan's global meridional circulation system. Approximate lifetimes for these species are on the order of a few years, which matches the stratospheric chemical/dynamical lifetimes (at $z = 300$ km) predicted by the latest chemical models for Titan's atmosphere, indicating that their dominant production and loss mechanisms are reasonably well understood. The HCN and CH_3CN maps show polar peaks with reduced contrast compared with the other species, implying that they are relatively more well mixed in latitude, consistent with the longer lifetimes of these gases (between about half and a few Saturnian years).

Limb flux profiles confirm that CH_3CN tends to be one of the more abundant nitriles at lower (stratospheric) altitudes, whereas the HC_3N abundance in the stratosphere is low and rises sharply with altitude throughout the mesosphere. The HNC vertical abundance profile is unique among the gases measured, as it does not become detectable until altitudes $\gtrsim$700 km in Titan's thermosphere. Thus, ground-based observations of HNC provide a unique probe of the high-altitude chemical and physical processes occurring in Titan's thermosphere/ionosphere.

The ALMA HNC map shows significant longitudinal asymmetry. This is explained as a result of the combined effects of zonal winds and diurnal variations in the ionospheric $HCNH^+$ abundance, which is theorized to be lower on the night side due to reduced solar insolation, giving rise to a reduced HNC abundance at the western (dawn) limb. The observed east–west asymmetry confirms the very rapid theorized production and loss rates for this species (on the order of a day at 1000 km altitude), making HNC a unique probe of short-timescale ionospheric processes.

This work was supported by the National Science Foundation under grant No. AST-1616306, the NASA Astrobiology Institute (NAI), the NASA Solar System Observations program, and the UK Science and Technology Facilities Council (STFC). It makes use of ALMA data set ADS/JAO. ALMA#2016.A.00014.S. ALMA is a partnership of ESO (representing its member states), NSF (USA), and NINS (Japan), together with NRC (Canada), and NSC and ASIAA (Taiwan), in cooperation with the Republic of Chile. The Joint ALMA Observatory is operated by ESO, AUI/NRAO, and NAOJ. The National Radio Astronomy Observatory is a facility of the National Science Foundation operated under cooperative agreement by Associated Universities, Inc.

Appendix
Limb Flux Profile Fits

Least-squares fits to the equatorial fluxes as a function of (sky-projected) radius are shown in Figure 9, using a simple,

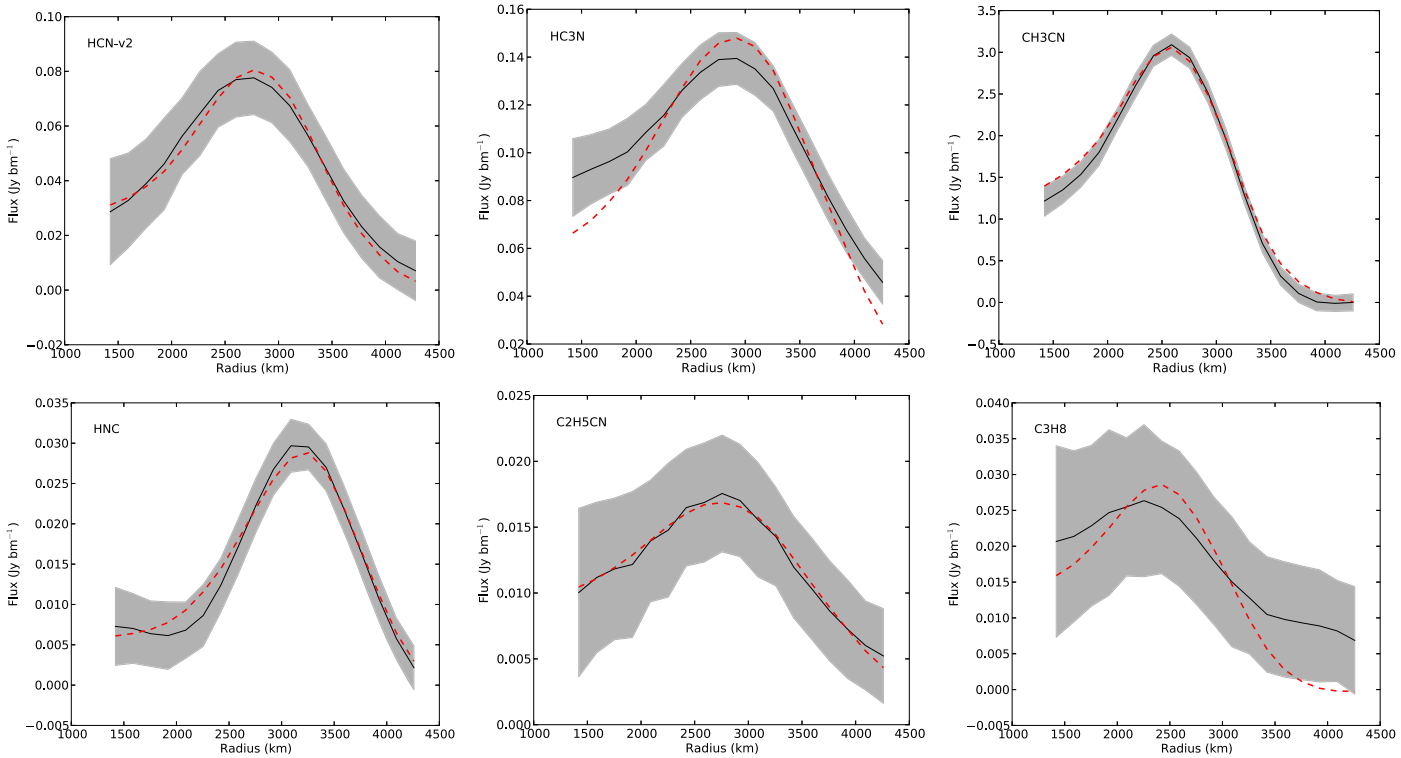

Figure 9. Peak-normalized equatorial limb flux profiles observed using ALMA (excluding the regions within ±45° of Titan's north and south poles). Gray envelopes indicate 1σ flux uncertainties, and the best-fitting model profiles are shown using red dashed curves. Radial distances are with respect to the center of Titan's disk, projected in the plane of the sky.

four-parameter model (two parameters for C_3H_8) for the abundance of each species (x) as a function of altitude (z). See Section 4.4 for details of the modeling procedure. The corresponding optimized $x(z)$ profiles are shown in Figure 6.

ORCID iDs

M. A. Cordiner https://orcid.org/0000-0001-8233-2436
N. A. Teanby https://orcid.org/0000-0003-3108-5775
C. A. Nixon https://orcid.org/0000-0001-9540-9121
V. Vuitton https://orcid.org/0000-0001-7273-1898
A. E. Thelen https://orcid.org/0000-0002-8178-1042

References

Achterberg, R. K., Gierasch, P. J., Conrath, B. J., Michael Flasar, F., & Nixon, C. A. 2011, Icar, 211, 686
Adriani, A., Dinelli, B. M., López-Puertas, M., et al. 2011, Icar, 214, 584
Bézard, B., Yelle, R., & Nixon, C. 2014, in Titan: Surface, Atmosphere and Magnetosphere, ed. I. Muller-Wodarg et al. (Cambridge: Cambridge Univ. Press), 158
Boucher, D., Burie, J., Bauer, A., Dubrulle, A., & Demaison, J. 1980, JPCRD, 9, 659
Brauer, C. S., Pearson, J. C., Drouin, B. J., & Yu, S. 2009, ApJS, 184, 133
Cordiner, M. A., Nixon, C. A., Charnley, S. B., et al. 2018, ApJL, 859, L15
Cordiner, M. A., Nixon, C. A., Teanby, N. A., et al. 2014, ApJL, 795, L30
Cordiner, M. A., Palmer, M. Y., Nixon, C. A., et al. 2015, ApJL, 800, L14
Coustenis, A., Bampasidis, G., Achterberg, R. K., et al. 2013, ApJ, 779, 177
Coustenis, A., & Bézard, B. 1995, Icar, 115, 126
Coustenis, A., Salama, A., Schulz, B., et al. 2003, Icar, 161, 383
Cravens, T. E., Robertson, I. P., Waite, J. H., et al. 2009, Icar, 199, 174
Cui, J., Galand, M., Yelle, R. V., et al. 2009, JGRA, 114, A06310
Dobrijevic, M., Loison, J. C., Hickson, K. M., & Gronoff, G. 2016, Icar, 268, 313
Drouin, B. J., Pearson, J. C., Walters, A., & Lattanzi, V. 2006, JMoSp, 240, 227
Flasar, F. M., Kunde, V. G., Abbas, M. M., et al. 2004, SSRv, 115, 169
Hörst, S. M. 2017, JGRE, 122, 432
Hubbard, W. B., Sicardy, B., Miles, R., et al. 1993, A&A, 269, 541
Irwin, P. G. J., Teanby, N. A., de Kok, R., et al. 2008, JQSRT, 109, 1136
Jaeger, S. 2008, in ASP Conf. Ser. 394, Astronomical Data Analysis Software and Systems XVII, ed. R. W. Argyle, P. S. Bunclark, & J. R. Lewis (San Francisco, CA: ASP), 623
Jennings, D. E., Flasar, F. M., Kunde, V. G., et al. 2017, ApOpt, 56, 5274
Kisiel, Z., Pszczółkowski, L., Drouin, B. J., et al. 2009, JMoSp, 258, 26
Krasnopolsky, V. A. 2009, Icar, 201, 226
Lai, J. C.-Y., Cordiner, M. A., Nixon, C. A., et al. 2017, AJ, 154, 206
Lellouch, E., Gurwell, M. A., Moreno, R., et al. 2019, NatAs, 3, 614
Loison, J. C., Hébrard, E., Dobrijevic, M., et al. 2015, Icar, 247, 218
Maguire, W. C., Hanel, R. A., Jennings, D. E., Kunde, V. G., & Samuelson, R. E. 1981, Natur, 292, 683
Markwardt, C. 2012, MPFIT: Robust non-linear least squares curve fitting, Astrophysics Source Code Library, ascl:1208.019
Molter, E. M., Nixon, C. A., Cordiner, M. A., et al. 2016, AJ, 152, 42
Moreno, R., Lellouch, E., Lara, L. M., et al. 2011, A&A, 536, L12
Moreno, R., Marten, A., & Hidayat, T. 2005, A&A, 437, 319
Müller, H. S. P., Thorwirth, S., Roth, D. A., & Winnewisser, G. 2001, A&A, 370, L49
Müller-Wodarg, I. C. F., Yelle, R. V., Mendillo, M., Young, L. A., & Aylward, A. D. 2000, JGR, 105, 20833
Nixon, C. A., Jennings, D. E., Flaud, J.-M., et al. 2009a, P&SS, 57, 1573
Nixon, C. A., Lorenz, R. D., Achterberg, R. K., et al. 2018, P&SS, 155, 50
Nixon, C. A., Teanby, N. A., Calcutt, S. B., et al. 2009b, ApOpt, 48, 1912
Palmer, M. Y., Cordiner, M. A., Nixon, C. A., et al. 2017, SciA, 3, e1700022
Shinnaga, H., Humphreys, E., Indebetouw, R., et al. 2015, in ASP Conf. Ser. 499, Revolution in Astronomy with ALMA: The Third Year, ed. D. Iono et al. (San Francisco, CA: ASP), 355
Teanby, N. A. 2007, MatG, 39, 419
Teanby, N. A., Bézard, B., Vinatier, S., et al. 2017, NatCo, 8, 1586
Teanby, N. A., Irwin, P. G. J., de Kok, R., et al. 2007, Icar, 186, 364
Teanby, N. A., Irwin, P. G. J., de Kok, R., et al. 2008, Icar, 193, 595
Teanby, N. A., Irwin, P. G. J., de Kok, R., & Nixon, C. A. 2009, RSPTA, 367, 697
Teanby, N. A., Irwin, P. G. J., Nixon, C. A., et al. 2012, Natur, 491, 732
Teanby, N. A., Sylvestre, M., Sharkey, J., et al. 2019, GeoRL, 46, 3079
Thelen, A. E., Nixon, C. A., Chanover, N. J., et al. 2018, Icar, 307, 380

Thelen, A. E., Nixon, C. A., Chanover, N. J., et al. 2019, Icar, 319, 417
Thorwirth, S., Müller, H. S. P., & Winnewisser, G. 2000, JMoSp, 204, 133
Vinatier, S., Bézard, B., Lebonnois, S., et al. 2015, Icar, 250, 95
Vinatier, S., Bézard, B., Nixon, C. A., et al. 2010, Icar, 205, 559
Vuitton, V., Yelle, R. V., Klippenstein, S. J., Hörst, S. M., & Lavvas, P. 2019, Icar, 324, 120
Willacy, K., Allen, M., & Yung, Y. 2016, ApJ, 829, 79
Wilson, E. H., & Atreya, S. K. 2004, JGRE, 109, 6002